

A Fermi-degenerate three-dimensional optical lattice clock

S.L. Campbell,^{1,2,*} R.B. Hutson,^{1,2,*} G.E. Marti,¹ A. Goban,¹ N. Darkwah Oppong,^{1,†} R.L. McNally,^{1,2,‡} L. Sonderhouse,^{1,2} J. Robinson,^{1,2} W. Zhang,^{1,§} B.J. Bloom,^{1,2,¶} and J. Ye^{1,2,**}

¹JILA, NIST and University of Colorado, 440 UCB, Boulder, Colorado 80309, USA

²Department of Physics, University of Colorado, Boulder, Colorado 80309, USA

(Dated: February 7, 2017)

Strontium optical lattice clocks have the potential to simultaneously interrogate millions of atoms with a spectroscopic quality factor $Q \approx 4 \times 10^{17}$. Previously, atomic interactions have forced a compromise between clock stability, which benefits from a large atom number, and accuracy, which suffers from density-dependent frequency shifts. Here, we demonstrate a scalable solution which takes advantage of the high, correlated density of a degenerate Fermi gas in a three-dimensional optical lattice to guard against on-site interaction shifts. Using a state-of-the-art ultra-stable laser, we achieve an unprecedented level of atom-light coherence, reaching $Q = 5.2 \times 10^{15}$ with 1×10^4 atoms. We investigate clock systematics unique to this design; in particular, we show that contact interactions are resolved so that their contribution to clock shifts is orders of magnitude lower than in previous experiments, and we measure the combined scalar and tensor magic wavelengths for state-independent trapping along all three lattice axes.

INTRODUCTION

Atomic clocks are advancing the frontier of measurement science, enabling tabletop searches for dark matter and physics beyond the Standard Model [1–3], while also providing innovative quantum technologies for other branches of science [4]. Modern atomic clocks serve as the backbone of global navigation systems and provide the basis for defining the SI base units [5]. Progress in atomic clocks is driven by improvements in the spectroscopic quality factor Q , single-particle quantum state control, and better characterization of systematic shifts [6–9].

One-dimensional (1D) optical lattice clocks provide a many-particle optical frequency reference that, together with advances in optical local oscillators, has led to record clock stability [10, 11] and the accompanying ability to evaluate systematic shifts to greater accuracy than ever before [12–14]. However, the need to avoid atomic interactions places increasingly challenging engineering constraints on 1D optical lattice systems [15–17]. A three-dimensional (3D) optical lattice was used in [18] to suppress atomic interactions in a clock based on a thermal gas of bosons. Moving forward, the knowledge and tools from the quantum gas community [19–22] can be used to prepare metrologically useful quantum matter, combining the benefits of both single-particle quantum state control and correlated many-particle systems.

Here, we implement the next step in optical lattice clock design: a degenerate Fermi gas in a 3D opti-

cal lattice. In this configuration, the atom number can be scaled by orders of magnitude, while strong interactions prevent systematic errors associated with high atomic density. Specifically, we load a two-spin degenerate Fermi gas into the ground band of a 3D optical lattice in the Mott-insulating regime where the number of doubly occupied sites is suppressed [20, 21, 23]. In a Mott insulator with one atom per site, the density is maximized while collisional frequency shifts are greatly suppressed. For any residual atoms in doubly occupied sites, the enhanced interaction energy in a 3D lattice ensures that their transitions are well-resolved from the unperturbed clock transitions for atoms in singly occupied sites. To reduce the limiting effects of trapping light on clock accuracy and stability, we measure the ac Stark shifts of the clock transition from the three orthogonal lattice beams to determine their respective magic wavelengths for state-independent trapping. With the contact interaction and lattice ac Stark shifts controlled, we observe coherent Ramsey fringes at a 6 s free evolution time with 1×10^4 atoms. We operate at a density above 10^{13} atoms/cm³, three orders of magnitude greater than in previous lattice clock experiments [14]. The work here takes an initial but important step towards reaching the ultimate limit of performance for strontium optical lattice clocks, where millions of atoms could be interrogated for coherence times greater than 100 s.

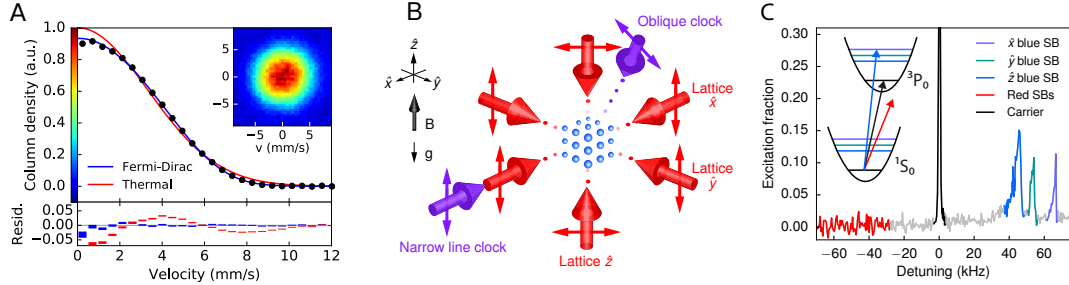


Fig. 1. A Fermi-degenerate 3D optical lattice clock. (A) Momentum distribution data of a two-spin Fermi gas after being released from the crossed optical dipole trap. The inset shows an absorption image of the freely expanding gas. The azimuthally averaged column density deviates from a Maxwell-Boltzmann fit, but agrees well with a Fermi-Dirac fit giving $T/T_F = 0.2$. (B) Schematic showing propagation direction (large arrows) and polarization (double arrows) of the 3D lattice and clock laser beams. The quantization axis is defined by the magnetic field B . The narrow line clock laser used for precision spectroscopy is phase-stabilized to lattice \hat{x} . The oblique clock laser is used drive motional sidebands along all three lattice axes. (C) Motional sideband spectroscopy using the oblique clock laser shows no observable red sidebands, illustrating that atoms are predominantly in the ground band of the lattice.

PREPARATION

Laser cooling followed by optical pumping to the $m_F = \pm 9/2$ stretched nuclear spin states produces a two-spin Fermi gas with an initial phase space density of 0.1 in a crossed optical dipole trap. Evaporative cooling to degeneracy proceeds by exponentially decreasing the trap depth in a 7 s, two-stage ramp [24, 25]. For different measurement goals, we optimize particular final parameters such as temperature (10 to 60 nK) and atom number (10^4 to 10^5). Fig. 1A shows a freely expanding degenerate Fermi gas of 4×10^4 atoms. The temperature T and Fermi temperature T_F are determined from a fit to the Fermi-Dirac distribution, giving $T = 60$ nK and $T/T_F = 0.2$.

The atoms are then adiabatically loaded from the crossed optical dipole trap into the ground band of a 3D optical lattice. As the lattice depth rises, the increasing role of interactions relative to tunneling suppresses multiple occupancies in the Mott-insulating regime. At the final lattice depths of 40 to 100 E_{rec} , where E_{rec} is the lattice photon recoil energy, the Lamb-Dicke requirement is satisfied for clock light along all directions [26]. Spectroscopy is performed on the 698 nm 1S_0 ($|g; m_F\rangle$) \leftrightarrow 3P_0 ($|e; m_F\rangle$) clock transition. As shown in Fig. 1B, the clock laser propagating along the \hat{x} lattice beam is used for precision spectroscopy, while an oblique clock laser enables a systematic characterization of the lattice via motional sideband spectroscopy (see Fig. 1C). The absence of observable red-

detuned sidebands demonstrates that the atoms are predominantly loaded into the ground band of the 3D lattice.

ATOMIC INTERACTIONS

In the ground band of the lattice, each site can be occupied by either one atom, or by two atoms with opposite nuclear spin. Tight confinement in the 3D lattice gives rise to strong interactions on doubly occupied sites. We label the two-particle eigenstates of the two-orbital interaction Hamiltonian as $|gg; m_F, m'_F\rangle = |gg\rangle \otimes |s\rangle$, $|eg^+; m_F, m'_F\rangle = (|eg\rangle + |ge\rangle)/\sqrt{2} \otimes |s\rangle$, $|eg^-; m_F, m'_F\rangle = (|eg\rangle - |ge\rangle)/\sqrt{2} \otimes |t\rangle$, and $|ee; m_F, m'_F\rangle = |ee\rangle \otimes |t\rangle$ with corresponding energies U_{gg} , U_{eg}^+ , U_{eg}^- , and U_{ee} [27–30]. Here, $|s\rangle$ and $|t\rangle$ represent the singlet and triplet wavefunctions for the two spins, m_F and m'_F . An applied magnetic bias field mixes the $|eg^+; m_F, m'_F\rangle$ and $|eg^-; m_F, m'_F\rangle$ states due to a differential Landé g -factor between the two orbitals. We label the new eigenstates of the combined interaction and Zeeman Hamiltonian as $|eg^u; m_F, m'_F\rangle$ and $|eg^d; m_F, m'_F\rangle$.

Clock light resonantly couples the ground state $|gg; m_F, m'_F\rangle$ only to the states $|eg^{u,d}; m_F, m'_F\rangle$. The energies U_{eg}^+ and U_{eg}^- differ from U_{gg} on the $h\text{-kHz}$ scale, where h is the Planck constant, resulting in transitions on doubly occupied sites that are well-resolved from the single-atom clock transitions and strong suppression of two-photon transitions to the $|ee; m_F, m'_F\rangle$

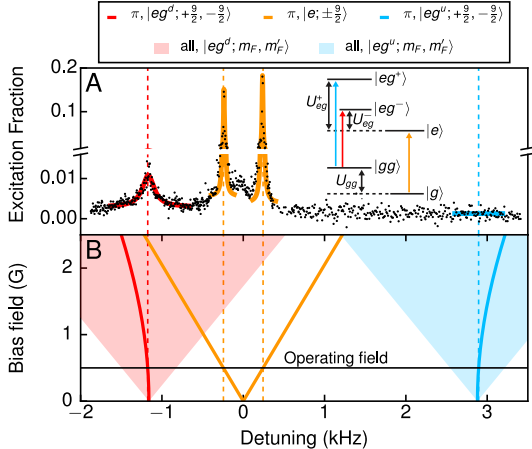


Fig. 2. Resolved atomic contact interactions. (A) Clock spectroscopy data of a two-spin Fermi gas in the $m_F = \pm 9/2$ stretched states for a 500 mG magnetic field, where a small fraction of the lattice sites contain both spin states. All transitions are saturated. The $|gg; -9/2, 9/2\rangle \rightarrow |eg^u; -9/2, 9/2\rangle$ transition is absent due to its vanishing dipole matrix element at small magnetic fields. Inset: Level diagram at zero magnetic field. (B) Calculated detunings for transitions on singly and doubly occupied sites. The solid lines correspond to transitions on singly occupied (orange) and doubly occupied (red, blue) sites with $m_F = \pm 9/2$. Transitions on doubly occupied sites for arbitrary m_F and clock laser polarization lie within the shaded regions. At our operating magnetic field of 500 mG, all resonances for doubly occupied sites are well-resolved from the clock transitions.

state. In 1D optical lattice clocks, interaction shifts are less than clock transition Rabi frequencies; in 2D clocks, interaction shifts and Rabi frequencies are comparable [31]. In contrast, the interaction shifts in a 3D lattice are 10^3 times greater than the clock transition Rabi frequency. Although for normal clock operation we load at most one atom per site, to measure contact interactions we increase the final Fermi temperature so that a small fraction of lattice sites are filled with two atoms in the $|gg; +9/2, -9/2\rangle$ state. Fig. 2A shows clock spectroscopy for a magnetic field $B = 500$ mG. At this field, π -polarized clock light gives a negligible transition amplitude to the $|eg^u; +9/2, -9/2\rangle$ state due to destructive interference between the two oppositely signed transition dipole moments for the stretched states. Therefore, we observe excitation to the $|eg^d; +9/2, -9/2\rangle$ state, highlighted in red, and no excitation to the $|eg^u; +9/2, -9/2\rangle$ state, highlighted

in blue.

Clock operation predominantly probes atoms in singly occupied sites, with only a negligible systematic shift due to line pulling caused by transitions from the few atoms in doubly occupied sites. For a comprehensive study of line pulling from doubly occupied sites, we use our measurements of $U_{eg}^- - U_{gg}$ and $U_{eg}^+ - U_{gg}$ at $B = 0$ to calculate the spectrum of all transitions on doubly occupied sites as a function of B , as shown in Fig. 2B (see Supplementary Materials, SM). We account for imperfect clock laser polarization and residual spin populations by considering π, σ^+ , and σ^- transitions to all $|eg^{u,d}; m_F, m'_F\rangle$ states, as indicated in the shaded regions in Fig. 2B. At intermediate magnetic fields, transitions from doubly occupied sites can cross clock transitions and potentially cause significant frequency shifts. However, this is avoided if B is kept sufficiently low. At our chosen bias field of 500 mG [12, 14], transitions on doubly occupied sites are at least 500 Hz away. From a 1% upper bound on residual transition amplitudes, we estimate the fractional frequency shift due to line pulling effects from doubly occupied sites to be below 1×10^{-24} for 1 Hz linewidths (see SM). We also calculate the fractional frequency shifts due to superexchange interactions [32] between neighboring sites at typical lattice depths and find them to be below 1×10^{-22} .

While on-site interaction shifts can be eliminated in 3D lattice clocks, atoms may also interact via long-range electric dipole forces, which can lead to many-body effects such as collective frequency shifts, superradiance, and subradiance [33]. At unit filling, clock shifts from dipolar interactions could reach the 10^{-18} level [34, 35], though employing different 3D lattice geometries is a promising approach for canceling these shifts. Exploring different strategies for accurately measuring and eliminating dipolar frequency shifts will be a fruitful avenue of future study.

3D MAGIC WAVELENGTH

There has been a long-standing question as to whether the overall ac Stark shift in a 3D lattice can be managed to allow state-of-the-art narrow line clock spectroscopy. We implement a solution to this challenge, inspired by the proposal in [36]. The differential ac Stark shift from the lattice trapping beams at a particular trap depth U_0 can be expressed in terms of its

scalar, vector, and tensor components as [36, 37],

$$\Delta\nu = (\Delta\kappa^s + \Delta\kappa^v m_F \xi \hat{e}_k \cdot \hat{e}_B + \Delta\kappa^t \beta) U_0, \quad (1)$$

where $\Delta\kappa^{s,v,t}$ are the scalar, vector, and tensor shift coefficients, respectively, ξ is the lattice light ellipticity, and \hat{e}_k and \hat{e}_B are unit vectors along the lattice beam wave vector and magnetic field quantization axis, respectively. The parameter β can be expressed as $\beta = (3\cos^2\theta - 1)[3m_F^2 - F(F+1)]$, where θ is the angle between the nearly-linear lattice polarization and \hat{e}_B .

We achieve state-independent trapping by operating the lattice at the combined scalar and tensor magic wavelength and ensuring that the vector shift is zero [14, 38]. Linearly polarized lattice light ($\xi = 0$) suppresses the vector shift, and the tensor shift is minimally sensitive to drifts in θ when the polarization either parallel ($\theta = 0^\circ$) or perpendicular ($\theta = 90^\circ$) to the quantization axis. The frequency of the trapping light is then tuned to adjust the scalar shift so that it precisely cancels the tensor component. The $\theta = 0^\circ$ configuration has been thoroughly studied in 1D lattice clocks [14, 38]. For the 3D lattice, we set the horizontal (\hat{x}, \hat{y}) and vertical (\hat{z}) lattice polarizations to be parallel and perpendicular to \hat{e}_B , respectively, as shown in Fig. 1B. The two polarization configurations have distinct magic frequencies due to their different tensor shifts.

We measure the magic frequencies for the vertical and horizontal lattice beams. A continuous-wave Ti:Sapphire laser is used for the lattice light because of its low incoherent background [39]. The absolute frequency of the lattice laser is traceable to the UTC NIST timescale through an optical frequency comb. For a given lattice laser frequency, we measure the differential ac Stark shift using four interleaved digital servos that lock the clock laser frequency to the atomic resonance for alternating high and low lattice intensities and $m_F = \pm 9/2$ spin states [12, 14, 38]. From the data shown in Fig. 3, we measure that the vertical ($\theta = 90^\circ$) and horizontal ($\theta = 0^\circ$) magic frequencies are 368.554839(5) THz and 368.554499(8) THz, respectively, in agreement with [14, 38, 39]. From these two magic frequencies, we find that the scalar magic frequency is 368.554726(4) THz, in agreement with [39].

Since there are only two θ configurations with a stable tensor shift, in a 3D lattice two of the three lattice beams will necessarily have the same magic frequency.

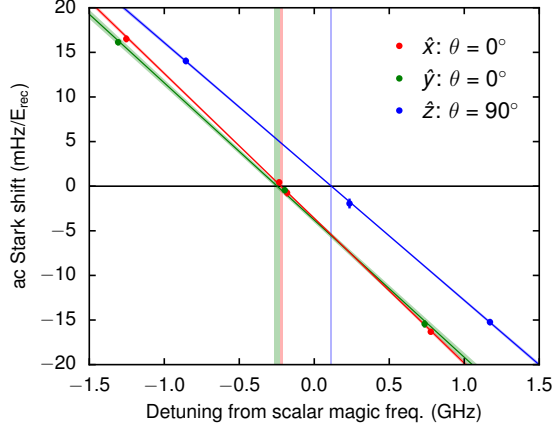


Fig. 3. State-independent trapping in a 3D optical lattice. Determination of the magic wavelengths for the horizontal (\hat{x}, \hat{y}) and vertical (\hat{z}) lattices, with $|m_F| = 9/2$. The vertical and horizontal lattices have distinct magic wavelengths due to their different tensor shifts arising from different angles θ between the lattice polarization and magnetic field quantization axes. For presentation, the measured frequency shift is scaled by the difference in peak trap depths at the high and low lattice intensities. The difference in slopes is caused by trapping potential inhomogeneities and does not affect the determination of the magic frequencies.

However, the frequencies of all lattice beams must be offset to avoid interference, which is known to cause heating in ultracold quantum gas experiments [40]. We choose our two horizontal beams to have the same polarization and operate them with equal and opposite detunings (± 2.5 MHz) from their magic frequency, giving equal and opposite ac Stark shifts from the two beams. From the slopes in Fig. 3, we determine that for a 10% imbalance in trap depths, detuning the two horizontal beams ± 2.5 MHz from their magic wavelength results in a $< 1 \times 10^{-18}$ systematic shift, the exact magnitude of which can be measured to much better accuracy.

Another issue resulting from our 3D geometry is that one lattice beam must operate with $\hat{e}_k \cdot \hat{e}_B = 1$, which can give rise to a vector ac Stark shift due to residual circular polarization. The vertical (\hat{z}) beam has this configuration, and we measure a $3 \times 10^{-18} \times m_F/E_{\text{rec}}$ vector shift, corresponding to an ellipticity of $\xi = 0.007$ [36]. In contrast, the horizontal beams (\hat{x}, \hat{y}) with $\hat{e}_k \cdot \hat{e}_B = 0$ enjoy an additional level of vector shift suppression. Nevertheless, the clock operates by

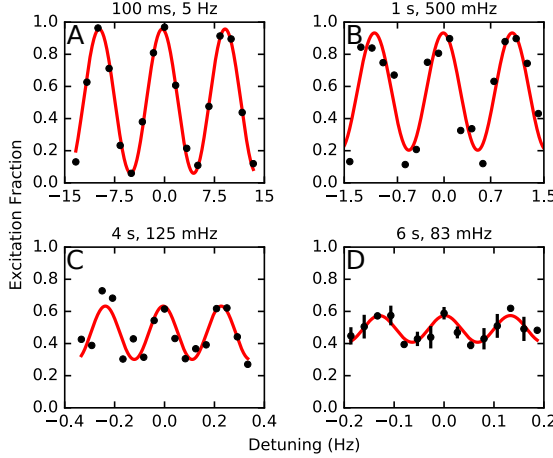


Fig. 4. Narrow-line clock spectroscopy. Ramsey spectroscopy data taken with 1×10^4 atoms at 15 nK for (A) 100 ms, (B) 1 s, (C) 4 s, and (D) 6 s free-evolution times, using 10 ms $\pi/2$ pulse times. With contact interactions and ac Stark shifts controlled in a 3D lattice, we are able to measure fringes at a record 6 s free-evolution time with a density of over 10^{13} atoms/cm³. The data shown in (D) is an average of two measurements, with 1σ error bars shown.

locking to alternating opposite spin states, so the net vector shift can be removed.

NARROW LINE SPECTROSCOPY

With atomic interactions and lattice ac Stark shifts controlled, we demonstrate a new record for narrow-line clock spectroscopy. Fig. 4 shows a progression of Ramsey fringes with free evolution times from 100 ms to 6 s, beyond what has been demonstrated in 1D lattice clocks [14, 17, 41]. The \hat{x} lattice beam is operated at a depth sufficient ($>80E_{\text{rec}}$) to prevent atoms from tunneling along the clock laser axis during the 6 s free evolution period. Spectroscopy is performed on a spin-polarized sample, prepared by first exciting $|g; -9/2\rangle \rightarrow |e; -9/2\rangle$, then removing all ground state atoms via resonant ${}^1S_0 - {}^1P_1$ light. Our longest observed coherence time approaches the limit of our clock laser based on its noise model [42] and the 12 s dead time between measurements. For the demonstration of Ramsey fringes at longer free-evolution times, maintaining atom-light phase coherence will require a significant reduction in fundamental thermal noise from the optical local oscillator. Additionally, the ob-

servation of narrower lines will require magnetic field control below the 100 μG level. The contrast of the observed Ramsey fringes is likely limited by lattice light causing both dephasing over the atomic sample and excited state population decay. Inhomogeneities are minimized for our smallest samples with an atom number of 1×10^4 and temperature of 15 nK.

CONCLUSION

Optical lattice clocks have now entered the quantum degenerate regime. With atoms that are frozen into a 3D cubic lattice, we have advanced the state-of-the-art in coherent atom-light interrogation times. Further improvements will be enabled by the next generations of ultra-stable optical reference cavities based on crystalline materials [43, 44]. The latest advances in the frequency references and local oscillators that together constitute atomic clocks will lead to a new era for clock performance, resulting in new measurement capabilities [45].

Quantum degenerate clocks also provide a promising platform for studying many-body physics. Future studies of dipolar interactions will not only be necessary for clock accuracy, but will also provide insight into long-range quantum spin systems in a regime distinct from those explored by polar molecules [46, 47], Rydberg gases [48, 49], and highly magnetic atoms [50–53]. When clocks ultimately confront the natural linewidth of the atomic frequency reference, degenerate Fermi gases may be useful for engineering longer coherence times through Pauli blocking of spontaneous emission [54] or collective radiative effects [35, 55]. Ultracold quantum gases provide new capabilities for precision metrology.

ACKNOWLEDGMENTS

We thank D.E. Chang and H. Ritsch for insightful discussions on dipolar interactions in a 3D lattice. We also acknowledge technical contributions and discussions from C. Benko, T. Bothwell, S.L. Bromley, K. Hagen, J.L. Hall, B. Horner, H. Johnson, T. Keep, S. Kolkowitz, J. Levine, T.H. Loftus, T.L. Nicholson, E. Oelker, D.G. Reed, and X. Zhang. This work is supported by NIST, DARPA, and the NSF JILA Physics Frontier Center. G.E.M. is supported by a National Research Council Postdoctoral Fellowship, A.G. is sup-

ported by a JSPS Fellowship, and L.S. is supported by a NDSEG fellowship.

* These authors contributed equally to this work.

† Present address: Ludwig-Maximilians-Universität, Schellingstraße 4, 80799 München, Germany and Max-Planck-Institut für Quantenoptik, Hans-Kopfermann-Straße 1, 85748 Garching, Germany

‡ Present address: Department of Physics, Columbia University, 538 West 120th Street, New York, New York 10027-5255, USA

§ Present address: National Institute of Standards and Technology (NIST), Boulder, Colorado 80305, USA

¶ Present address: Rigetti Computing, 775 Heinz Avenue, Berkeley, CA 94710

** Corresponding author. E-mail: ye@jila.colorado.edu

- [1] K. Van Tilburg, N. Leefer, L. Bougas, and D. Budker, Physical Review Letters **115**, 011802 (2015).
- [2] A. Arvanitaki, J. Huang, and K. Van Tilburg, Physical Review D **91**, 015015 (2015).
- [3] Y. V. Stadnik and V. V. Flambaum, Physical Review A **93**, 063630 (2016).
- [4] A. D. Ludlow, M. M. Boyd, J. Ye, E. Peik, and P. Schmidt, Reviews of Modern Physics **87**, 637 (2015).
- [5] T. J. Quinn, Philosophical Transactions of the Royal Society A: Mathematical, Physical and Engineering Sciences **369**, 3905 (2011).
- [6] D. J. Wineland, Reviews of Modern Physics **85**, 1103 (2013).
- [7] S. Haroche, Reviews of Modern Physics **85**, 1083 (2013).
- [8] N. Huntemann, C. Sanner, B. Lipphardt, C. Tamm, and E. Peik, Physical Review Letters **116**, 063001 (2016).
- [9] R. Wynands and S. Weyers, Metrologia **42**, S64 (2005).
- [10] T. L. Nicholson, M. J. Martin, J. R. Williams, B. J. Bloom, M. Bishop, M. D. Swallows, S. L. Campbell, and J. Ye, Physical Review Letters **109**, 230801 (2012).
- [11] N. Hinkley, J. A. Sherman, N. B. Phillips, M. Schioppo, N. D. Lemke, K. Beloy, M. Pizzocaro, C. W. Oates, and A. D. Ludlow, Science **341**, 1215 (2013).
- [12] B. J. Bloom, T. L. Nicholson, J. R. Williams, S. L. Campbell, M. Bishop, X. Zhang, W. Zhang, S. L. Bromley, and J. Ye, Nature **506**, 71 (2014).
- [13] I. Ushijima, M. Takamoto, M. Das, T. Ohkubo, and H. Katori, Nature Photonics **9**, 185 (2015).
- [14] T. L. Nicholson, S. L. Campbell, R. B. Hutson, G. E. Marti, B. J. Bloom, R. L. McNally, W. Zhang, M. D. Barrett, M. S. Safronova, G. F. Strouse, W. L. Tew, and J. Ye, Nature Communications **6**, 6896 (2015).
- [15] G. K. Campbell, M. M. Boyd, J. W. Thomsen, M. J. Martin, S. Blatt, M. D. Swallows, T. L. Nicholson, T. Fortier, C. W. Oates, S. A. Diddams, N. D. Lemke, P. Naidon, P. Julienne, J. Ye, and A. D. Ludlow, Science **324**, 360 (2009).
- [16] N. D. Lemke, J. von Stecher, J. A. Sherman, A. M. Rey, C. W. Oates, and A. D. Ludlow, Physical Review Letters **107**, 103902 (2011).
- [17] M. J. Martin, M. Bishop, M. D. Swallows, X. Zhang, C. Benko, J. Von-Stecher, A. V. Gorshkov, A. M. Rey, and J. Ye, Science **341**, 632 (2013).
- [18] T. Akatsuka, M. Takamoto, and H. Katori, Physical Review A **81**, 023402 (2010).
- [19] B. DeMarco and D. S. Jin, Science **285**, 1703 (1999).
- [20] R. Jordens, N. Strohmaier, K. Gunter, H. Moritz, and T. Esslinger, Nature **455**, 204 (2008).
- [21] U. Schneider, L. Hackermüller, S. Will, T. Best, I. Bloch, T. A. Costi, R. W. Helmes, D. Rasch, and A. Rosch, Science **322**, 1520 (2008).
- [22] T. Rom, T. Best, D. van Oosten, U. Schneider, S. Fölling, B. Paredes, and I. Bloch, Nature **444**, 733 (2006).
- [23] M. Greiner, O. Mandel, T. Esslinger, T. W. Hänsch, and I. Bloch, Nature **415**, 39 (2002).
- [24] B. J. DeSalvo, M. Yan, P. G. Mickelson, Y. N. Martinez de Escobar, and T. C. Killian, Physical Review Letters **105**, 030402 (2010).
- [25] S. Stellmer, R. Grimm, and F. Schreck, Physical Review A **87**, 013611 (2013).
- [26] P. Lemonde and P. Wolf, Physical Review A **72**, 033409 (2005).
- [27] A. V. Gorshkov, M. Hermele, V. Gurarie, C. Xu, P. S. Julienne, J. Ye, P. Zoller, E. Demler, M. D. Lukin, and A. M. Rey, Nature Physics **6**, 289 (2010).
- [28] X. Zhang, M. Bishop, S. L. Bromley, C. V. Kraus, M. S. Safronova, P. Zoller, A. M. Rey, and J. Ye, Science **345**, 1467 (2014).
- [29] F. Scazza, C. Hofrichter, M. Höfer, P. C. De Groot, I. Bloch, and S. Fölling, Nature Physics **10**, 779 (2014).
- [30] G. Cappellini, M. Mancini, G. Pagano, P. Lombardi, L. Livi, M. Siciliani de Cumis, P. Cancio, M. Pizzocaro, D. Calonico, F. Levi, C. Sias, J. Catani, M. Inguscio, and L. Fallani, Physical Review Letters **113**, 120402 (2014).
- [31] M. D. Swallows, M. Bishop, Y. Lin, S. Blatt, M. J. Martin, A. M. Rey, and J. Ye, Science **331**, 1043 (2011).
- [32] S. Trotzky, P. Cheinet, S. Flölling, M. Feld, U. Schnorrberger, A. M. Rey, A. Polkovnikov, E. A. Demler, M. D. Lukin, and I. Bloch, Science **319**, 295 (2008).
- [33] S. L. Bromley, B. Zhu, M. Bishop, X. Zhang, T. Bothwell, J. Schachenmayer, T. L. Nicholson, R. Kaiser, S. F. Yelin, M. D. Lukin, A. M. Rey, and J. Ye, Nature Communications **7**, 11039 (2016).
- [34] D. E. Chang, J. Ye, and M. D. Lukin, Physical Review A **69**, 023810 (2004).
- [35] S. Krämer, L. Ostermann, and H. Ritsch, Europhysics Letters **114**, 14003 (2016).
- [36] P. G. Westergaard, J. Lodewyck, L. Lorini, A. Lecalier, E. A. Burt, M. Zawada, J. Millo, and P. Lemonde, Physical Review Letters **106**, 210801 (2011).

- [37] M. M. Boyd, T. Zelevinsky, A. D. Ludlow, S. Blatt, T. Zanon-Willette, S. M. Foreman, and J. Ye, Physical Review A **76**, 022510 (2007).
- [38] S. Falke, N. Lemke, C. Grebing, B. Lipphardt, S. Weyers, V. Gerginov, N. Huntemann, C. Hagemann, A. Al-Masoudi, S. Häfner, S. Vogt, U. Sterr, and C. Lisdat, New Journal of Physics **16**, 073023 (2014).
- [39] C. Shi, J.-L. Robyr, U. Eismann, M. Zawada, L. Lorini, R. Le Targat, and J. Lodewyck, Physical Review A **92**, 012516 (2015).
- [40] M. Greiner, *Ultracold quantum gases in three-dimensional optical lattice potentials*, Ph.D. thesis, Ludwig-Maximilians-Universität München (2003).
- [41] M. Schioppo, R. C. Brown, W. F. McGrew, N. Hinkley, R. J. Fasano, K. Beloy, T. H. Yoon, G. Milani, D. Nicolodi, J. A. Sherman, N. B. Phillips, C. W. Oates, and A. D. Ludlow, “Ultra-stable optical clock with two cold-atom ensembles,” (2016), in press (<http://arxiv.org/abs/1607.06867>).
- [42] M. Bishop, X. Zhang, M. J. Martin, and J. Ye, Physical Review Letters **111**, 093604 (2013).
- [43] T. Kessler, C. Hagemann, C. Grebing, T. Legero, U. Sterr, F. Riehle, M. J. Martin, L. Chen, and J. Ye, Nature Photonics **6**, 687 (2012).
- [44] G. D. Cole, W. Zhang, M. J. Martin, J. Ye, and M. Aspelmeier, Nature Photonics **7**, 644 (2013).
- [45] S. Kolkowitz, I. Pikovski, N. Langellier, M. D. Lukin, R. L. Walsworth, and J. Ye, “Gravitational wave detection with optical lattice atomic clocks,” (2016), in press (<http://arxiv.org/abs/1606.01859>).
- [46] B. Yan, S. A. Moses, B. Gadway, J. P. Covey, K. R. A. Hazzard, A. M. Rey, D. S. Jin, and J. Ye, Nature **501**, 521 (2013).
- [47] S. A. Moses, J. P. Covey, M. T. Miecnikowski, B. Yan, B. Gadway, J. Ye, and D. S. Jin, Science **350**, 659 (2015).
- [48] P. Schauß, J. Zeiher, T. Fukuhara, S. Hild, M. Cheneau, T. Macrì, T. Pohl, I. Bloch, and C. Gross, Science **347**, 1455 (2015).
- [49] H. Labuhn, D. Barredo, S. Ravets, S. de Léséleuc, T. Macrì, T. Lahaye, and A. Browaeys, Nature **534**, 667 (2016).
- [50] K. Aikawa, S. Baier, A. Frisch, M. Mark, C. Ravensbergen, and F. Ferlaino, Science **345**, 1484 (2014).
- [51] A. de Paz, P. Pedri, A. Sharma, M. Efremov, B. Naylor, O. Gorceix, E. Maréchal, L. Vernac, and B. Laburthe-Tolra, Physical Review A **93**, 021603 (2016).
- [52] H. Kadau, M. Schmitt, M. Wenzel, C. Wink, T. Maier, I. Ferrier-Barbut, and T. Pfau, Nature **530**, 194 (2016).
- [53] N. Q. Burdick, Y. Tang, and B. L. Lev, Physical Review X **6**, 031022 (2016).
- [54] R. M. Sandner, M. Müller, A. J. Daley, and P. Zoller, Physical Review A **84**, 043825 (2011).
- [55] L. Ostermann, H. Ritsch, and C. Genes, Physical Review Letters **111**, 123601 (2013).
- [56] W. B. Dress, P. D. Miller, J. M. Pendlebury, P. Perrin, and N. F. Ramsey, Phys. Rev. D **15**, 9 (1977).
- [57] M. Swallows, *A search for the permanent electric dipole moment of mercury-199*, Ph.D. thesis, University of Washington (2007).
- [58] A. Law and W. D. Kelton, *Simulation Modeling and Analysis*, 3rd ed. (McGraw-Hill, New York, 2000).

3D Lattice Design

SUPPLEMENTARY MATERIALS

Materials and Methods

In an ultrahigh vacuum chamber with a >90 s background gas collision-limited lifetime, we perform initial laser cooling of ^{87}Sr in a magneto-optical trap (MOT) on the 30 MHz $^1S_0 - ^1P_1$ transition. We then load atoms into a second-stage MOT which operates on the 7 kHz $^1S_0 - ^3P_1$ intercombination transition. For evaporative cooling, the atoms are next loaded into a 1064 nm crossed optical dipole trap (XODT), which is formed by a horizontal and a vertical beam crossing at their respective waists. The XODT is held on throughout both the broadband and narrow-line cooling stages in the second-stage MOT. To ensure that narrow-line cooling works efficiently inside the XODT, the spatially dependent differential ac Stark shifts of the $^1S_0 - ^3P_1$ cooling transition must be minimized.

The horizontal beam has a sheetlike geometry with waists of 340 μm and 17 μm in the horizontal and vertical directions, respectively. By focusing more tightly in the vertical direction, the horizontal beam achieves the same confinement against gravity for a lower light intensity. The vertical beam, which is aligned at a small angle with respect to gravity, is a circular Gaussian beam with a 64 μm beam waist. Similar to [25], the vertical beam is circularly polarized to minimize differential ac Stark shifts. We perform a further stage of cooling by blue-detuning the cooling light relative to the free space resonance to address atoms inside the XODT.

After the MOT is switched off, 5×10^6 atoms at 1.5 μK are loaded into the XODT, in an equal mixture of all 10 nuclear spin states. To prepare an equal mixture of the stretched $m_F = \pm 9/2$ states, we perform optical pumping via the $^1S_0 \leftrightarrow ^3P_1, F = 9/2$ transition in a 3 G magnetic bias field, which splits neighboring m_F states by 260 kHz. First, a σ^- -polarized optical pumping beam is frequency-chirped from the $m_F = 1/2 \rightarrow 3/2$ transition to the $m_F = 7/2 \rightarrow 9/2$ transition, which pumps all $m_F < 0$ atoms into the $m_F = -9/2$ state. In the second step, a liquid crystal waveplate is used to switch the laser polarization to σ^+ , and similarly all the $m_F > 0$ atoms are pumped into the $m_F = 9/2$ state.

First, we consider both the requirements for adiabatic loading into the ground band of the lattice and for reaching the Mott-insulating regime. Loading the ground band requires that $E_F, k_B T \ll E_{\text{rec}}$, where E_F is the Fermi energy, k_B is the Boltzmann constant, T is the temperature, and E_{rec} is the recoil energy from a lattice photon. Competition between tunneling (J) and repulsive interactions (U) initializes the spatial distribution of the atoms. As the lattice depth increases, multiple occupancies are suppressed when $12J \ll U$ and $k_B T \ll E_F \ll U$ [20, 21].

Next, we consider how finite tunneling rates affect clock spectroscopy. We require $1/J_x \gg \tau$, where J_x is the tunneling rate along the clock laser propagation direction and τ is the spectroscopy time, as the finite Bloch bandwidth of the lattice potential causes a first-order Doppler broadening of $8J_x$. This requirement is satisfied for our longest spectroscopy times $\tau = 6$ s by using lattice depths above $80E_{\text{rec}}$. To achieve a sufficiently deep trap as well as mode-match with the XODT, we use elliptical beams for the \hat{x} and \hat{y} lattice axes with horizontal and vertical waists of 120 μm and 35 μm , respectively. The \hat{z} lattice beam is round with a 90 μm waist. Typical operating parameters in our experiment are summarized in Table S1, and a list of the requirements on these experimental parameters is summarized in Table S2.

Interactions and Line Pulling

We calculate the detunings of transitions from doubly occupied sites, relative to the single-atom clock transition $|g; m_F\rangle \rightarrow |e; m_F\rangle$ at zero magnetic field. Since the clock operates under a magnetic bias field B , we consider how competing Zeeman and interaction energies determine the energy eigenstates for atoms on doubly occupied sites with arbitrary m_1 and m_2 . The Zeeman shifts for $|g; m_F\rangle$ and $|e; m_F\rangle$ are $g_I \mu_B B m_F$ and $(g_I + \delta g) \mu_B B m_F$, where g_I is the nuclear g -factor ($g_I \mu_B = h \cdot 184.4 \text{ Hz/Gauss}$) and δg is the differential g -factor between the ground and clock states ($\delta g \mu_B = h \cdot 108.4 \text{ Hz/Gauss}$). The differential Zeeman shift between the two clock states introduces a coupling between the $|eg^+; m_1, m_2\rangle$ and $|eg^-; m_1, m_2\rangle$ states. Thus, the combined interaction and differential Zeeman Hamiltonian in the $|eg^\pm; m_1, m_2\rangle$ basis can be

Parameter	Symbol	Typical Value
Fermi energy	E_F	$75 \text{ nK}\cdot k_B$
Temperature	T	15 nK
Lattice recoil energy	$E_{\text{rec},\text{lattice}}$	$167 \text{ nK}\cdot k_B$
Clock laser recoil energy	$E_{\text{rec},\text{clock}}$	$226 \text{ nK}\cdot k_B$
Contact interaction energies	U	$2 \text{ kHz}\cdot h$
Bloch bandwidth	$4J$	$6 \times 10^{-7} E_{\text{rec},\text{lattice}}$
Tunneling rate along the clock laser axis	J_x/h	0.5 mHz
Spectroscopy time	τ	6 s
Trap depth	$\mathcal{U}_{0,x}, \mathcal{U}_{0,y}, \mathcal{U}_{0,z}$	$(100, 70, 50) E_{\text{rec},\text{lattice}}$
Trap frequency	ν_x, ν_y, ν_z	$(65, 55, 45) \text{ kHz}$

TABLE S1. Typical operating parameters.

Requirement	Inequality
Ground band loading	$E_F, k_B T \ll E_{\text{rec},\text{lattice}}$
Double occupancy suppression	$J \ll U, k_B T \ll E_F \ll U$
Resolved contact interactions	$\Delta U \gg 1/\tau$
Lamb-Dicke	$h\nu \gg E_{\text{rec},\text{clock}}$
Doppler suppression	$8J_x/h \ll 1/\tau$

TABLE S2. Requirements for clock operation in a Mott-insulating regime with one atom per site.

expressed as [28, 29]:

$$\hat{H} = \begin{pmatrix} U_{eg}^+ + \frac{\Delta_1 + \Delta_2}{2} & \frac{\Delta_1 - \Delta_2}{2} \\ \frac{\Delta_1 - \Delta_2}{2} & U_{eg}^- + \frac{\Delta_1 + \Delta_2}{2} \end{pmatrix}, \quad (\text{S1})$$

where $\Delta_{1,2} = \delta g \mu_B B m_{1,2}$ are the differential Zeeman shifts. The two eigenstates $|eg^u; m_1, m_2\rangle$ and $|eg^d; m_1, m_2\rangle$ have eigenenergies given by,

$$E_{\{u,d\}}(m_1, m_2) = V + \frac{\Delta_1 + \Delta_2}{2} \pm \sqrt{V_{\text{ex}}^2 + \left(\frac{\Delta_1 - \Delta_2}{2}\right)^2}, \quad (\text{S2})$$

where $V = (U_{eg}^+ + U_{eg}^-)/2$ and $V_{\text{ex}} = (U_{eg}^+ - U_{eg}^-)/2$ are the direct and exchange interaction energies, respectively. The detunings of the $|gg; m_1, m_2\rangle \rightarrow |eg^{\{u,d\}}; m'_1, m'_2\rangle$ transitions relative

to the $B = 0$ single-atom clock transition are,

$$\begin{aligned} \Delta E_{\{u,d\}}(m_1, m_2; m'_1, m'_2) &= E_{\{u,d\}}(m'_1, m'_2) \\ &\quad - U_{gg} + g_I \mu_B B (m'_1 + m'_2 - m_1 - m_2), \end{aligned}$$

when the two-particle Rabi couplings $\Omega^{\{u,d\}}(m_1, m_2; m'_1, m'_2; q)$ with $\pi(q = 0)$ or $\sigma^\pm(q = \mp 1)$ -polarized clock light are non-zero, as discussed below.

The atom-light Hamiltonian for a single particle driven by $\pi(\sigma^\pm)$ -polarized clock light is given by,

$$\hat{H}_q^{(1)} = \frac{\hbar}{2} \sum_{m_F} (\Omega_{m_F, q} |e; m_F - q\rangle \langle g; m_F| + \text{h.c.}), \quad (\text{S3})$$

Here, the single-particle coupling $\Omega_{m_F, q}$ is expressed using the Wigner-Eckart theorem as,

$$\Omega_{m_F, q} = -\langle F_g, m_F; 1, q | F_e, m_F - q \rangle \langle F_g || d || F_e \rangle \cdot \frac{\mathcal{E}_q}{\hbar}, \quad (\text{S4})$$

where $\langle F_g || d || F_e \rangle$ is the reduced matrix element and \mathcal{E}_q is the electric field amplitude. Then, the two-particle atom-light Hamiltonian is written as,

$$\hat{H}_q^{(2)} = \left(\hat{H}_q^{(1)} \right)_1 \otimes (\mathbb{1})_2 + (\mathbb{1})_1 \otimes \left(\hat{H}_q^{(1)} \right)_2. \quad (\text{S5})$$

We find the two-particle couplings $\Omega^\pm(m_1, m_2; m'_1, m'_2; q)$ between the $|gg; m_1, m_2\rangle$ and $|eg^\pm; m'_1, m'_2\rangle$ transitions, driven by $\pi(q=0)$ - or $\sigma^\pm(q=\mp 1)$ -polarized clock beams to be,

$$\begin{aligned} \frac{\hbar}{2}\Omega^\pm(m_1, m_2; m'_1, m'_2; q) &= \langle eg^\pm; m'_1, m'_2 | \hat{H}_q^{(2)} | gg; m_1, m_2 \rangle \\ &= \frac{\hbar}{2\sqrt{2}} \left[\{ \Omega_{m_1, q} (\delta_{m'_1, m_1-q} \delta_{m'_2, m_2} \mp \delta_{m'_1, m_2} \delta_{m'_2, m_1-q}) + \Omega_{m_2, q} (\pm \delta_{m'_1, m_1} \delta_{m'_2, m_2-q} - \delta_{m'_1, m_2-q} \delta_{m'_2, m_1}) \} \right. \\ &\quad \left. (1 - \delta_{m'_1, m'_2}) + \sqrt{2}(\Omega_{m_1, q} \delta_{m'_1, m_1-q} \delta_{m'_1, m_2} - \Omega_{m_2, q} \delta_{m'_1, m_1} \delta_{m'_1, m_2-q}) \delta_{m'_1, m'_2} \right]. \end{aligned} \quad (\text{S6})$$

Thus, the two-particle couplings $\Omega^{\{u,d\}}(m_1, m_2; m'_1, m'_2; q)$ between the $|gg; m_1, m_2\rangle$ and $|eg^{\{u,d\}}; m'_1, m'_2\rangle$ states at a given B are obtained from linear combinations of Eq. S6. Fig. S1 shows all the detunings $\Delta E_{\{u,d\}}(m_1, m_2; m'_1, m'_2)$ from Eq. S6 for non-zero $\Omega^{\{u,d\}}(m_1, m_2; m'_1, m'_2; q)$ with π (black lines), σ^+ (red lines), and σ^- (blue lines) clock laser polarizations, as well as all single-atom transitions. In the case of an equal mixture of $m_F = \pm 9/2$ stretched states, the π -polarized clock light does not drive the $|gg; 9/2, -9/2\rangle \rightarrow |eg^+; 9/2, -9/2\rangle$ transition, since $\Omega_{m_1=9/2, q=0} = -\Omega_{m_2=-9/2, q=0}$ gives zero coupling strength as seen in Eq. S6. At our operating B , $|eg^u\rangle \approx |eg^+\rangle$, so π -polarized clock light only drives the $|gg; 9/2, -9/2\rangle \rightarrow |eg^d; 9/2, -9/2\rangle$ transition, as shown in Fig. 2A.

Next, we investigate line pulling effects due to the additional lines shown in Fig. S1. Single-particle line pulling effects have already been discussed in [38]; here we focus on line pulling from transitions on doubly occupied sites. We approximate the lineshapes as Lorentzians with full width at half maximum Γ . For typical clock operation, the error signal ε for the digital PID that steers the clock laser center frequency f_0 to the atomic resonance is generated by measuring the normalized excitation fraction N_{exc} at $f_0 + \Gamma/2$ and at $f_0 - \Gamma/2$ [12, 14]. The clock frequency is locked to the atomic reference such that $\varepsilon = N_{\text{exc}}(f_0 - \Gamma/2) - N_{\text{exc}}(f_0 + \Gamma/2) = 0$. In Fig. S2, we study how an additional line with a given amplitude relative to the clock transition modifies the center frequency f_0 for which $\varepsilon = 0$. Transitions from atoms on doubly occupied sites begin to overlap with the clock transitions

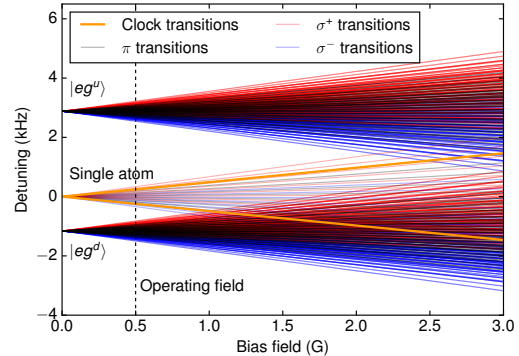


Fig. S1. All transitions from singly and doubly occupied sites. Detunings (relative to the unperturbed clock transition) for all transitions that can be driven on singly and doubly occupied lattice sites, shown for typical trap depths. Fig. 3B in the main text is a simplified version of this figure, with the shaded regions covering the range of all lines, and the solid lines showing the transition frequencies for only the states with $m_F = \pm 9/2$.

when $B > (U_{gg} - U_{eg}^-)/[(9\delta g + g_I)\mu_B]$. At our chosen bias field of 500 mG [12, 14], the transitions on doubly occupied sites are separated from the main clock transitions by at least 500 Hz. Using a 1% upper bound on residual transition amplitudes and assuming 1 Hz transition linewidths, we estimate the fractional frequency shift due to line pulling effects from doubly occupied sites to be below 1×10^{-24} .

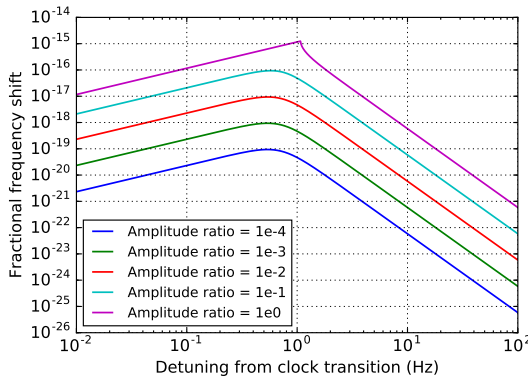


Fig. S2. Line pulling. Systematic shifts due to line pulling from a residual line. Though the linewidth of the residual line will vary depending on what transition is being driven, we perform this calculation for 1 Hz linewidths to give a reasonable upper bound. The amplitude ratio indicates the amplitude of the residual line relative to that of the clock transition.

3D Magic Wavelength

We evaluate the ac Stark shift using four interleaved but independent servos locked to the $m_F = \pm 9/2$ transitions for each of the high and low lattice intensity configurations, with high and low lattice depths differing by approximately $30E_{\text{rec}}$. Each servo tracks the detuning between one transition of the strontium atoms and the TEM00 mode of an ultra-stable cavity [17].

Laser frequency drift gives a nonuniform shift to the interleaved locks that can lead to an erroneous offset in the measured ac Stark shift. Every four experimental cycles, we measure independent frequencies locked to the four configurations $\{f_{\text{high},+9/2}^i, f_{\text{low},+9/2}^i, f_{\text{high},-9/2}^i, f_{\text{low},-9/2}^i\}$, where high and low refer to lattice depths, $\pm 9/2$ refer to the m_F states, and i is the iteration number of the experiment. A four-point string analysis [56, 57] removes linear and quadratic laser drift using the following linear combination of eight consecutive measurements:

$$\Delta f_{\text{scalar+tensor}}^i = \frac{3}{16} (f_{\text{high},+9/2}^i + f_{\text{high},-9/2}^i) - \frac{5}{16} (f_{\text{low},+9/2}^i + f_{\text{low},-9/2}^i) + \frac{5}{16} (f_{\text{high},+9/2}^{i+1} + f_{\text{high},-9/2}^{i+1}) - \frac{3}{16} (f_{\text{low},+9/2}^{i+1} + f_{\text{low},-9/2}^{i+1}), \quad (\text{S7})$$

$$\Delta f_{\text{vector}}^i = \frac{3}{16} (f_{\text{high},+9/2}^i - f_{\text{high},-9/2}^i) - \frac{5}{16} (f_{\text{low},+9/2}^i - f_{\text{low},-9/2}^i) + \frac{5}{16} (f_{\text{high},+9/2}^{i+1} - f_{\text{high},-9/2}^{i+1}) - \frac{3}{16} (f_{\text{low},+9/2}^{i+1} - f_{\text{low},-9/2}^{i+1}). \quad (\text{S8})$$

The measured frequencies are correlated in time because the servos low-pass filter the system response. We correct the servo frequency using the error signal, which contains higher-frequency components of the system response, according to,

$$f_{\text{corrected}} = f_{\text{uncorrected}} + \frac{\Gamma}{2A} \times e, \quad (\text{S9})$$

where Γ is the FWHM linewidth, e is the error signal (the difference between the excitation fraction from probing the left and right sides of the line), and A is the maximum peak height of the spectroscopic feature. Fig. S3 demonstrates that this procedure flattens the autocorrelation function of the corrected data (blue) com-

pared to the uncorrected data (green). To estimate the autocorrelation function from the data, we use the formula [58],

$$\rho_j = \frac{\sum_{i=1}^{n-j} [X_i - \bar{X}(n)][X_{i+j} - \bar{X}(n)]}{(n - j)S^2(n)} \quad (\text{S10})$$

$$S^2(n) = \frac{\sum_{i=1}^n [X_i - \bar{X}(n)]^2}{n(n - 1)}. \quad (\text{S11})$$

We use the autocorrelation function to calculate the un-

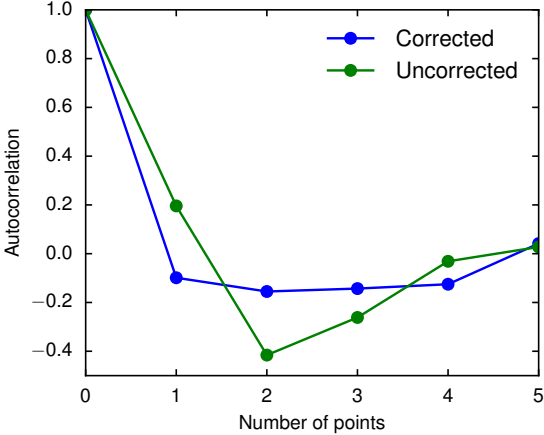


Fig. S3. Autocorrelation plot. Autocorrelation functions of the measured ac Stark shifts for clock laser servo frequencies uncorrected (green) and corrected by the measured error signal (blue).

biased error for correlated data,

$$\frac{\sigma}{\sqrt{n}} \sqrt{1 + 2 \sum_{j=1}^{n-1} \left(1 - \frac{j}{n}\right) \rho_j}, \quad (\text{S12})$$

where σ is the standard deviation of the point-string difference frequencies Δf^i , ρ_j is the autocorrelation function for data separated by j points, and n is the number of measured frequencies [58].

All of these steps are validated on simulated data modeled by clock laser noise similar to the actual laser [42], with a power spectral density $S \propto 1/f$, where f is the frequency, and a linear frequency drift from imperfectly canceled material creep of the reference cavity between -2 and 2 mHz/s. We use weighted least-squares fitting to determine the magic wavelength for each lattice direction. From the difference in the splittings between the $\pm 9/2$ states for the high and low lattice intensities, we also extract the vector ac Stark shift, as shown in Fig. S4.

Narrow line spectroscopy

Using Rabi spectroscopy with a 4 s pulse time, we measure a full-contrast Fourier-limited linewidth of 190(20) mHz, as shown in Fig. S5. This is different

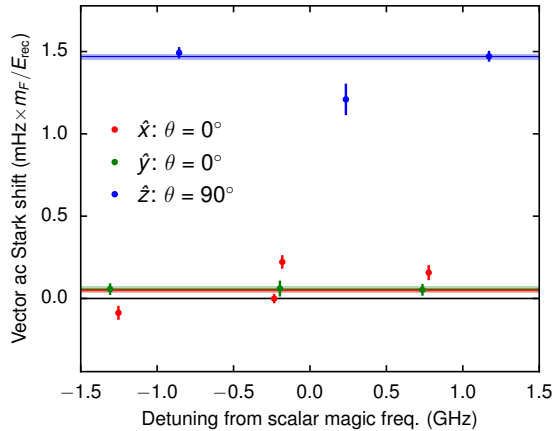


Fig. S4. Vector ac Stark shift. Measuring the vector ac Stark shift for the horizontal (\hat{x} , \hat{y}) and vertical (\hat{z}) configurations. The vector shift from the vertical lattice beam is sensitive to a small ellipticity in the polarization because $\hat{e}_k \cdot \hat{e}_B = 1$, while the horizontal beams with $\hat{e}_k \cdot \hat{e}_B = 0$ benefit from additional suppression of the vector shift.

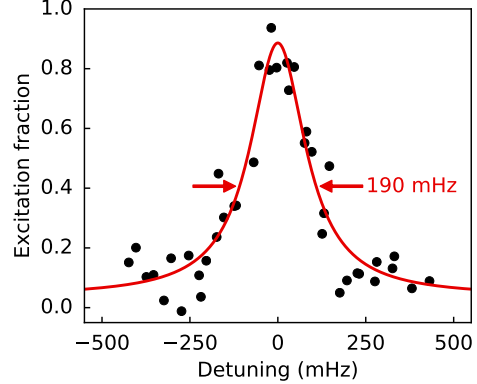


Fig. S5. Narrow-line Rabi spectroscopy. Rabi spectroscopy data for a 4 s π -pulse time, showing a 190(20) mHz Fourier-limited linewidth, taken with $m_F = 9/2$ and rescaled by the relative spin population.

than spectroscopy in a 1D lattice, where clock scans at the longest probe times show substantially reduced contrast due to atomic contact interactions [14, 17].